Experimental Electron Density in Crystalline H₃PO₄

By Mohamed Souhassou*

Medical Foundation of Buffalo, 73 High Street, Buffalo, NY 14203, USA

Enrique Espinosa

Laboratoire de Minéralogie-Cristallographie et Physique Infrarouge, Faculté des Sciences, Université de Nancy I, URA-CNRS 809, Bôite Postale No. 239, 54506 Vandoeuvre-lès-Nancy CEDEX, France, and Institut de Ciècia de Materials de Barcelona, Consejo Superior de Investigaciones Cientificas, Campus de la Universitat Autonoma de Barcelona, 08193 Bellaterra (Barcelona), Spain

Claude Lecomte

Laboratoire de Minéralogie-Cristallographie et Physique Infrarouge, Faculté des Sciences, Université de Nancy I, URA-CNRS 809, Bôite Postale No. 239, 54506 Vandoeuvre-lès-Nancy CEDEX, France

and Robert H. Blessing†

Medical Foundation of Buffalo, 73 High Street, Buffalo, NY 14203, USA, and Laboratoire de Minéralogie-Cristallographie et Physique Infrarouge, Faculté des Sciences, Université de Nancy I, URA-CNRS 809, Bôite Postale No. 239, 54506 Vandoeuvre-lès-Nancy CEDEX, France

Abstract

X-ray diffraction data for H_3PO_4 crystals have been measured to $d_{min} = 0.46$ Å resolution, and used to model the electron-density distribution with the hydrogen structure of the crystals adopted from an earlier neutron diffraction analysis. The molecule is asymmetric in the crystal with site symmetry 1 (C_1), but the local symmetries of the pseudoatomic densities are, within experimental error, equivalent as they would be under idealized $3m$ (C_{3v}) molecular symmetry. Although the experimental analysis entailed substantial problems with absorption and extinction corrections, the static deformation density from the experiment agrees very well with that from a polarized split-valence molecular orbital wavefunction for an isolated molecule with the crystallographic molecular geometry. Hydrogen bonding in the crystal polarizes the molecule's P=O acceptor group towards P^+—O^-, and appears to relocalize the lone-pair density of the P—OH donor groups. Crystal data: anhydrous orthophosphoric acid, H_3PO_4, $M_r = 98.00$, room temperature, $P2_1/c$, $a = 5.7572$ (13), $b = 4.8310$ (17), $c = 11.5743$ (21) Å, $\beta = 95.274$ (12)°, $V = 320.55$ (25) Å³, $Z = 4$, $d_x = 2.030$ mg mm⁻³, $\mu = 0.660$ mm⁻¹ for λ(Mo $K\alpha$) = 0.7107 Å, $F(000) = 200$ e⁻, $R(|F|) = 0.026$ for 3512 unique reflections.

Introduction

An accompanying paper (Moss, Souhassou, Espinosa, Lecomte & Blessing, 1995) reports computational studies of the electron-density distribution in crystalline H_3PO_4. This paper reports a corresponding experimental analysis based on high-resolution X-ray diffraction data. The X-ray data were measured at room temperature so that mean positions and anisotropic mean-square displacements for the hydrogen nuclei could be adopted from an earlier analysis (Blessing, 1988, 1989a) of room-temperature neutron data. We are interested in the electron distribution and chemical bonding in H_3PO_4 because it is the prototype of biochemical phosphates, in particular, those involved in the ATP cycle of bioenergetics.

Experimental

Masses of single crystals of orthophosphoric acid, H_3PO_4, were found in a jar of commercial (Fluka Chemical Corporation) pyrophosphoric acid, $H_4P_2O_7$, and identified by X-ray diffraction. Evidently, during storage the extremely hygroscopic solid pyro-acid had captured enough water vapor to hydrolyze to, and recrystallize as, the ortho-acid. The ortho-acid crystals, which are also very hydroscopic, were immersed in toluene to protect them from atmospheric moisture while they were examined under an optical microscope, and selected specimens were quickly sealed in thin-walled glass capillaries for X-ray diffraction measurements. The

---

* Present address: Laboratoire de Minéralogie-Cristallographie et Physique Infrarouge, Faculté des Sciences, Université de Nancy I, URA-CNRS 809, Bôite Postale No. 239, 54506 Vandoeuvre-lès-Nancy CEDEX, France.

† To whom correspondence should be addressed.

crystals had the form of rectangular or square (001) tablets displaying (101), ($\bar{1}$01), (011) and (0$\bar{1}$1) faces in addition to (001) and (00$\bar{1}$). Many crystals were larger than $1 \times 1 \times 0.5$ mm. The specimen used for the diffraction measurements was about $0.75 \times 0.75 \times 0.30$ mm, but it was not possible to measure the dimensions very precisely, because the view of the crystal was obscured by its enclosing capillary and by a film of adhering liquid formed by slight dissolution in rapidly adsorbed atmospheric moisture, which obliterated the crystal's edges and vertices. The adhering liquid was quite viscous and cemented the crystal to the wall of the capillary so that the capillary axis was displaced from and inclined to the goniostat spindle axis.

Diffraction data were measured with Zr-filtered Mo X-rays on an Enraf–Nonius CAD-4 diffractometer, using its option for minimum absorption orientation of a flat-plate specimen. Reflection profiles were recorded as $\omega/2\theta$ scans for the full sphere of reflections with $|h| \leq 12$, $|k| \leq 10$, $|l| \leq 25$, and $(\sin\theta) \leq 1.09$ Å^{-1}. Scan widths were $\Delta\omega = 1.0° + 0.38° \tan\theta$, which correspond to approximately twice the base width of the reflection peaks, and the scan speed was a constant $d\omega/dt = 1.26°$ min^{-1}, which corresponded to ~50 reflection measurements per hour. The X-ray tube take-off angle was $2.9°$ so that the 'fine focus' 0.4×8 mm target focal spot was effectively a 0.4 mm square source, at a radius of 216.5 mm. The diameter of the incident beam-guide aperture was sufficient for a crystal of 1.3 mm diameter to have an unobstructed view of the whole effective focal spot. The detector aperture was a constant 4 (vertical) $\times$ 4 mm (horizontal) at a radius of 174 mm, which is equivalent to 1.3 (polar) $\times$ 1.3° (equatorial). Lattice parameters were determined by least-squares fit to the optimized setting angles of 25 reflections with θ values of ~25°.

Data reduction and error analysis (Blessing, 1989b, and references therein) included correction for the structured background under low-angle reflections due to the Zr K absorption edge of the β-filter (Nelmes, 1975). Seven reflections, (800), (0$\bar{4}$0), (008), (0,0,12), (00$\bar{8}$), (4$\bar{4}$7), and (3$\bar{3}$7), were remeasured at ~4 h intervals as intensity stability monitors. Least-squares curves fitted to the monitor data gave time-dependent scale factors that varied from 1.000 to 1.136 over the 282 h of X-ray exposure. Random fluctuations about the time-scaling curves gave $p = 0.0092$ for the error estimates $\sigma^2(|F|)^2 = [\sigma^2_{meas} + (p|F|^2)^2]^{1/2}$, where σ^2_{meas} was from propagation-of-error calculations that included Poisson counting statistics and an estimated scan angle uncertainty $\sigma(\omega) = 0.005°$. The p value corresponding to excess statistical scatter $< 1\%$ was satisfactorily small despite the almost 14% time-scale variation. This variation was not due to significant crystal decay or radiation damage, but rather to a period of stormy weather that affected power stability, laboratory air conditioning, crystal orientation and electronic perfor-

mance. Especially badly affected measurements detected during averaging of equivalent data were deleted.

Absorption corrections were applied in two stages. First, a correction was calculated by Gaussian numerical quadrature (DeTitta, 1985) over a $12 \times 12 \times 12$ grid using our best estimates of the dimensions of the crystal $[\mu(\text{Mo } K\alpha) = 0.660$ mm$^{-1}]$ and including correction for absorption by the capillary [1 mm diameter, 0.01 mm wall thickness, commercial soda-lime 'Glaskapillaren' with $\mu(\text{Mo } K\alpha) = 1.058$ mm$^{-1}]$. This yielded transmission factors $0.567 \leq A \leq 0.823$ and improved the internal agreement among equivalent measurements and their averages from $R_{merge} = \Sigma||F|^2 - \langle|F|^2\rangle|/ \Sigma|F|^2 = 0.0212$ before the absorption correction to 0.0186. Then, to correct for the imprecise data on the crystal dimensions and capillary dimensions and orientation, a refinement of the absorption correction was calculated by a least-squares fit of even-order real spherical harmonic functions, y_{lm} with $l_{max} = 8$, to the empirical transmission surface defined by the multiple symmetry-equivalent and azimuth rotation-equivalent measurements (Blessing, 1995). This yielded further corrections corresponding to effective transmission factors $0.897 \leq A \leq 1.099$ and further improved R_{merge} to 0.0182. The R_{merge} values are for averaging a total of 14 784 measurements to a set of 3512 unique data, of which 2785 had $|F|^2 \geq 3\sigma(|F|^2)$. Bayesian statistical treatment (French & Wilson, 1978) was applied to improve the estimates of $|F|^2$, $\sigma(|F|^2)$, $|F|$ and $\sigma(|F|)$ for the weak reflections, and all the unique data were used in the least-squares structure refinements.

As a check on the empirical absorption correction, it was also computed without the correction by Gaussian quadrature. This test yielded $0.518 \leq A \leq 0.823$ and $R_{merge} = 0.0190$, and the resulting test dataset agreed with the final dataset to within a least-squares scale factor of 0.92408 (12) and $R_{merge} = 0.0054$ between the two sets of unique data. Applicability of the empirical procedure depended on the greater than fourfold redundancy of equivalent measurements, which provided a thorough sampling of transmission paths through the crystal and capillary. The equivalent measurements included the instrumentally accessible settings at azimuths $\psi = 0, 15, 30, \ldots, 180°$ for the ($1\bar{6}1$), ($2\bar{6}1$), ($3\bar{5}5$), ($4\bar{5}3$), ($1,3,\bar{1}3$), ($7\bar{2}1$), ($0\bar{4}0$), ($3\bar{3}7$) and ($4\bar{4}7$) reflections, in addition to the general (hkl), $(h\bar{k}l)$, $(hk\bar{l})$ and $(\bar{h}kl)$ settings equivalent under the $2/m$ Laue symmetry.

Preliminary spherical-atom analysis

An initial set of spherical-atom least-squares refinements with the X-ray data was carried out using the neutron results as the starting model. The function minimized was $\chi^2 = \Sigma w(|F_o|^2 - k^{-2}y|F_c|^2)^2$ with $w = 1/\sigma^2(|F_o|^2)$. A one-parameter Darwin–Zachariasen extinction correction (Zachariasen, 1967) was applied by

the function $y = (1 + 2x)^{-1/2}$, where $x = gp_zLp|F_c|^2$ and $p_z = 2[1 + (\cos 2\theta)^4]/[1 + (\cos 2\theta)^2]^2$. The extinction parameter refined to $g = 0.506\ (21) \times 10^{-4}$. There were only 24 reflections with $y \leq 0.9$, but in the worst case, $y = 0.48$ for the $(\bar{1}02)$ reflection, the extinction was severe.

Refinement of the scale, extinction, positional and mean-square displacement parameters (anisotropic for P and O and isotropic for H), with all the data converged at $R_w = [\chi^2/\Sigma w(|F_o|^2)^2]^{-1/2} = 0.0599$, $R = R_w|_{w=1} = 0.0502$ and $Z = [\chi^2/(n - m)]^{1/2} = 1.731$ for $n = 3512$ data and $m = 59$ parameters. The non-H atoms were then further refined with the data with $(\sin\theta)/\lambda \geq 0.8\,\text{Å}^{-1}$, and this high-angle refinement converged at $R_w = 0.0562$, $R = 0.0342$ and $Z = 0.978$ for 2143 data and 46 parameters. The scale factor was very stable between the two refinements with $k^{-1} = 1.0596\,(14)$ and $1.063\,(4)$, respectively, and coordinates of the non-H atoms converged to the neutron results to within the estimated standard deviations of the differences. For the anisotropic mean-square displacements of the non-H atoms, the r.m.s. standardized difference between the X-ray and neutron values was $\langle(\Delta/\sigma)^2\rangle^{1/2} = 2.42$, where $\Delta/\sigma = (U_X^{ij} - U_N^{ij})/[\sigma^2(U_X^{ij}) + \sigma^2(U_N^{ij})]^{1/2}$.

A linear least-squares fit between the non-H U^{ij} from the high-angle X-ray refinement and those from the neutron analysis, minimizing $\chi^2 = \Sigma w[U_X^{ij} - (KU_N^{ij} + \Delta U^{ij})]^2$, with $w = 1/[\sigma^2(U_X^{ij}) + \sigma^2(U_N^{ij})]$, gave $Z = [\chi^2/(n - m)]^{1/2} = 1.18$ for the $n = 30$ pairs of U^{ij} values and the $m = 7$ parameters: $K = 1.027\,(20)$ and ΔU^{ij} ($ij = 11, 22, 33, 12, 13$ and 23) $= -0.0014\,(15)$, $-0.0024\,(6)$, $-0.0009\,(6)$, $-0.00002\,(22)$, $-0.00005\,(23)$ and $0.00188\,(24)\,\text{Å}^2$. These values from the non-H atoms were used to adjust the neutron U^{ij} values for the H atoms, and the H-atom coordinates and adjusted U^{ij} values from the neutron analysis were adopted as fixed parameters throughout the subsequent analysis.

At this point, after the high-angle $(\sin\theta)/\lambda \geq 0.8\,\text{Å}^{-1}$ refinement, a series of low-angle $(\sin\theta)/\lambda \leq 0.8\,\text{Å}^{-1}$ difference electron-density maps was prepared. These maps, which are deposited with the supplementary publication materials,* showed chemically reasonable density accumulations in bond and lone-pair regions and depletions in nonbonding regions.

Multipolar pseudoatom analysis

The valence electron distribution was fitted using the program *MOLLY* (Hansen & Coppens, 1978) and the pseudoatom model described in our accompanying paper (Moss *et al.*, 1995). Scattering factors for the core and

---

* A list of structure factors and supplementary density maps have been deposited with the IUCr (Reference: CR0476). Copies may be obtained through The Managing Editor, International Union of Crystallography, 5 Abbey Square, Chester CH1 2HU, England.

valence shells of spherically averaged free P and O atoms and for a spherically contracted ($\zeta = 1.15\,\text{bohr}^{-1}$) H atom (Stewart, Davidson & Simpson, 1965) were from atomic HF–SCF wavefunctions (Clementi, 1965). Anomalous dispersion corrections (Cromer, 1974) were added to the core scattering factors.

Noncrystallographic chemical constraints were imposed to minimize the number of pseudoatom parameters: Values of κ_0, P_v, κ_1 and P_{lm} were fitted for the four chemically distinct atom types P, O1, O2 (=O3 =O4) and H2 (=H3 =H4). Local atomic symmetries were assumed to be $3m\ (C_{3v})$ at the P atom, $\infty_m\ (C_{\infty v})$ at the O1 atom of the P=O group, $m\ (C_s)$ at the O2, O3 and O4 atoms of the P—OH groups, and $\infty_m\ (C_{\infty v})$ at the H atoms. The chemical and local atomic symmetry constraints were validated by comparing statistics-of-fit and residual difference densities from the constrained model with those from models with the constraints variously relaxed.

The pseudoatom least-squares refinements consisted of sequences of eight three-cycle stages. At each stage the parameters varied were the scale factor, the extinction parameters and the atomic parameters: (1) P_v, (2) κ_0, (3) P_v, (4) κ_0, (5) P_{lm}, (6) $\kappa_0 + \kappa_1$, (7) $P_v + P_{lm}$ and (8) non-H x_i and U^{ij}. The starting point was the converged spherical-atom model with the neutron-fixed H atom x_i and U^{ij}; the eight-stage sequence was reiterated several times; then, in a final two cycles, all parameters (except the H atom x_i and U^{ij}) were varied together.

The preliminary spherical-atom refinements had minimized an $|F|^2$ residual. The pseudoatom refinements minimized the $|F|$ residual $\chi^2 = \Sigma w \Delta^2$, where $\Delta = |F_o| - k^{-1}y^{1/2}|F_c|$ and $w = 1/\sigma^2(|F_o|)$. The statistics-of-fit, quoted below, were defined as $R = \Sigma|\Delta|/\Sigma|F_o|$, $R_w = [\chi^2/\Sigma w|F_o|^2]^{1/2}$, and $Z = [\chi^2/(n - m)]^{1/2}$, where $n = 3512$ data and $m = 80$ parameters, of which 33 were pseudoatom parameters. The fit was also judged by examining maps of the residual difference density $\Delta\rho(\mathbf{r}) = V^{-1}\Sigma_h(ky^{-1/2}|F_o| - |F_c|)\exp(i\varphi_c - 2\pi i\,\mathbf{h}\cdot\mathbf{r})$ compared with estimates of $\langle\sigma^2(\Delta\rho)\rangle^{1/2}$ given by $\sigma_1 = V^{-1}[\Sigma_h\sigma^2(ky^{-1/2}|F_o|)]^{1/2}$ and $\sigma_2 = V^{-1}[\Sigma_h(ky^{-1/2}|F_o| - |F_c|)^2]^{1/2}$ (Cruickshank, 1949). Anomalous dispersion effects were removed from the Fourier components of the density as described in the *Appendix*.

Results and discussion

Extinction effects

In the pseudoatom refinements, extinction was treated as secondary extinction due to an isotropic Lorentzian distribution of misorientations of mosaic blocks of isotropic dimensions (Becker & Coppens, 1974). Initially, a type I (mosaic spread dominated) model was assumed, and the extinction corrections converged to

very much the same values obtained earlier with the simplified Darwin–Zachariasen model in the preliminary spherical-atom refinements. Again there were only 24 reflections with $y \leq 0.9$, and the worst case was $y = 0.46$ for the (102) reflection. As shown in Fig. 1(a), however, this left unacceptably high levels of residual density after the pseudoatom fit. To no avail, we spent much effort searching for measurement errors or data processing mistakes that might account for the high residual density. Finally, we reconsidered the extinction model and found that a type (II) (block size dominated) model improved the statistics of fit and greatly reduced the residual density, as shown in Fig. 1(b). With the type (II) model there were 27 reflections with $y \leq 0.9$; the worst case was $y = 0.54$ for the (200) reflection; and the (102) reflection had $y = 0.59$.

With hindsight, we tested the two extinction types in spherical-atom refinements. Type (I) gave $R = 0.0332$, $R_w = 0.0329$, $Z = 1.88$; type (II) gave $R = 0.0323$, $R_w = 0.0323$, $Z = 1.85$. Thus, had we tested the extinction modeling in the preliminary spherical-atom refinements, we could have saved considerable time and effort in the pseudoatom refinements.

Residual densities

The final parameters corresponding to Fig. 1(b) are given in Tables 1 and 2, and sections of the corresponding static deformation density are shown in Fig. 2. Fig. 1(b) shows one of six sections of the residual density,
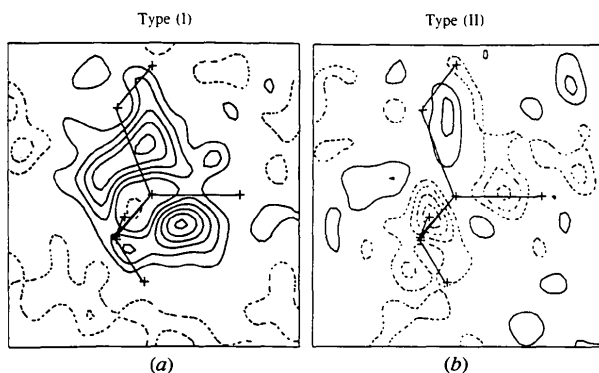
three (H—)O—P=O and three P—O—H sections, included in the deposited supplementary publication materials. The other two (H—)O—P=O sections are similar to Fig. 1(b), and the P—O—H sections are perhaps somewhat cleaner than the (H—)O—P=O sections. There is no indication in the residual maps that the imposed local chemical symmetry constraints were excessive. This was confirmed by several trial refinements with constraints relaxed, one atom at a time, to atomic site symmetry 1 (C_1), first for P, then for O1, and then for O4, which has a hydrogen-bond environment dissimilar to that of O2 and O3. None of these refinements significantly improved the statistics-of-fit or the residual maps.

Fig. 1(b) illustrates the most troublesome residual density features, namely, the minima of -0.2 and $-0.15 \, \mathrm{e \, \AA^{-3}}$ near the P atom along the P=O bond axis. These minima may be at least partly due to an inadequacy of the single-exponent $r^{n(l)} \, e^{-\alpha r}$, radial modeling of the P atom, since a similar, though shallower, pair of minima remained in the residual map [Fig. 3(b) of Moss et al. (1995)] corresponding to Fig. 1(b) after efforts to optimize the n_l and α of the P atom with simulated 'error-free' data.

Deformation density

The experimental static deformation density illustated in Fig. 2 strongly resembles the corresponding density from a polarized split-valence wavefunction [Figs. 2(a) and (b) of Moss et al. (1995)] and from a pseudoatom fit to structure factors simulated from the wavefunction [Fig. 4 of Moss et al. (1995)]. The principal differences are that the maximum along the P=O bond and the minimum near the P atom opposite the P=O bond are $\sim 0.1 \, \mathrm{e \, \AA^{-3}}$ lower in the experimental than in the theoretical density. Even if these differences are significant compared with errors of experimental measurement and theoretical approximation – as the residual densities discussed above suggest they might be – they
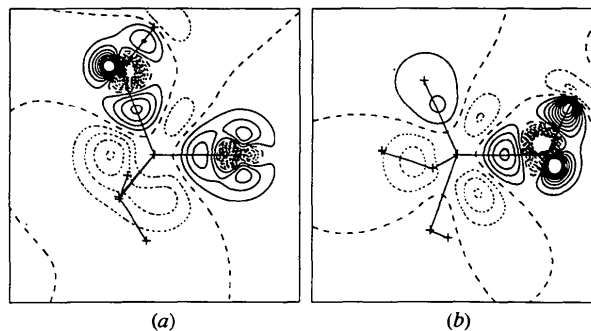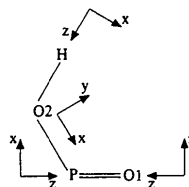

Fig. 1. Residual density in the (H—)O2—P=O plane after pseudoatom refinements with (a) type (I) and (b) type (II) secondary extinction models. The H atom is 0.43 Å out of the O—P=O plane. The Fourier sums included the 1313 terms with $(\sin \theta)/\lambda \leq 0.8 \, \mathrm{\AA^{-1}}$ and $|F_c| \geq 3\sigma(|F_o|)$. Contour interval 0.05 e Å^{-3}; solid contours for positive $\Delta \rho$; dotted for negative; zero contour omitted.

Refinement	Extinction parameter	R	R_w	Z	σ_1 (e Å^{-3})	σ_2 (e Å^{-3})
(a) Type (I)	$g\langle T \rangle = 0.0192\,(4) \times 10^4$	0.0273	0.0221	1.26	0.030	0.065
(b) Type (II)	$\rho\langle T \rangle = 0.0593\,(2) \times 10^4$	0.0257	0.0213	1.24	0.030	0.043

From our absorption calculations, the average value of the mean path length through the crystal was $\langle T \rangle = 0.045$ cm. Thus, for type (I), $g = 0.427 \times 10^4$ and the mean mosaic tilt is $\eta_L = (2\pi g)^{-1} = 7.7''$; for type (II), $\rho = 1.32 \times 10^4$ and the mean block size is $r = \rho \lambda = 0.93 \, \mu$m.

Fig. 2. Static deformation density in the planes (a) (H—)O2—P=O and (b) P—O2—H. In (a) the H atom is 0.43 Å above the O—P=O plane. Fig. 2 is to be compared with Fig. 2(a) and (b) of Moss et al. (1995). Contour interval 0.1 e Å^{-3}; positive contours solid, zero dashed and negative dotted.

Table 1. *Mean position and mean-square displacement parameters from the final pseudoatom refinement*

	x	y	z
H2	0.47077	0.61234	0.17676
H3	-0.13037	0.46585	0.16958
H4	0.26630	-0.05955	0.04327
O1	0.28348 (6)	0.16461 (8)	0.25344 (5)
O2	0.32284 (10)	0.58886 (10)	0.12898 (4)
O3	-0.05713 (9)	0.34091 (10)	0.11918 (5)
O4	0.27548 (7)	0.13198 (13)	0.03367 (5)
P	0.209186 (13)	0.300444 (16)	0.140186 (7)

	U^{11}	U^{22}	U^{33}	U^{12}	U^{13}	U^{23}
H2	0.03423	0.02833	0.03989	-0.00473	-0.00462	0.00005
H3	0.02602	0.04276	0.04228	0.00547	0.00003	-0.00681
H4	0.06616	0.03044	0.06918	0.00086	0.02257	-0.01438
O1	0.02172 (12)	0.02784 (13)	0.02510 (15)	-0.00112 (8)	-0.00243 (10)	0.00683 (14)
O2	0.02842 (15)	0.01557 (13)	0.03435 (17)	-0.00287 (13)	-0.00866 (22)	0.00255 (14)
O3	0.01671 (15)	0.03089 (16)	0.03196 (15)	0.00326 (12)	-0.00407 (12)	-0.00794 (24)
O4	0.03776 (29)	0.02212 (22)	0.02875 (17)	0.00407 (11)	0.00940 (17)	-0.00538 (15)
P	0.01619 (3)	0.01431 (3)	0.01952 (3)	0.001482 (20)	-0.001058 (20)	-0.000942 (24)

Table 2. *Pseudoatom parameters*

	κ_0	$\kappa_1\alpha$ (bohr^{-1})	α (bohr^{-1})	$l = 1, 2, 3, 4$
H	1.16 (3)	3.30 (22)	2.3	$n_l = 1, 2$
O1	0.971 (4)	4.4 (10)	4.5	2, 2
O2	0.991 (3)	6.9 (5)	4.5	2, 2, 3
P	0.992 (8)	4.7 (7)	4.7	6, 6, 7, 7

	P_v	$d11+$	$d11-$	$d10$	$q20$	$q21+$	$q21-$	$q22+$	$q22-$
H	0.81 (3)	0.0	0.0	0.108 (15)	0.076 (16)	0.0	0.0	0.0	0.0
O1	6.47 (5)	0.0	0.0	-0.042 (18)	-0.058 (16)	0.0	0.0	0.0	0.0
O2	6.17 (4)	0.007 (8)	-0.025 (9)	0.0	0.068 (16)	0.0	0.0	0.034 (10)	0.017 (9)

	$o30$	$o31+$	$o31-$	$o32+$	$o32-$	$o33+$	$o33-$
	0.0	0.057 (6)	0.059 (6)	0.0	0.0	0020 (5)	-0.002 (4)
P	0.0	0.0	0.054 (24)	-0.033 (22)	0.0	0.0	0.0
	0.498 (31)	0.0	0.0	0.0	0.0	0.379 (21)	-0.023 (14)

P 4.58 (11)

	$h40$	$h41+$	$h41-$	$h42+$	$h42-$	$h43+$	$h43-$	$h44+$	$h44-$
	0.048 (17)	0.0	0.0	0.0	0.0	-0.221 (16)	-0.031 (15)	0.0	0.0

The κ parameters are dimensionless and the α values are given in units of bohr^{-1}.

The form factor used for the H atoms was that for a spherically contracted atom with $\zeta = 1.15$ bohr^{-1}, so that the value $\kappa_0 = 1.16$ corresponds to $\kappa_0\alpha = 2\kappa_0\zeta = 2.67$ bohr^{-1}.

The functional form for each of the three dipoles, five quadruples, seven octopoles and nine hexadecapoles is as given by the respective entry in

are not large differences. Indeed, we think it remarkable that the pseudoatom model so effectively deconvolutes the static density from a dynamic structure that involves r.m.s. atomic displacements that on average exceed 0.15 Å.

Hydrogen-bonding effects

In the H$_3$PO$_4$ crystal structure [Fig. 1 of Moss *et al.* (1995)], the O1 atom of the P=O group accepts a pair of strong hydrogen bonds from neighboring P—OH groups, and the P=O($\cdots$H—O)$_2$ arrangement is close

to trigonal planar with O$\cdots$H distances of 1.55 and 1.59 Å. We therefore expected that we might see in the experimental deformation density a localization of O1 acceptor lone-pair density in directions corresponding to sp^2 hybrid orbitals directed toward the H—O donor groups. There was, however, no evidence in the residual maps of a significant departure from local cylindrical symmetry at O1.

Hydrogen-bonding effects are evident in differences between the valence geometry of the bound molecule in the crystal and the free molecule *in vacuo*, as summarized in Table 3. In the hydrogen-bonded

molecule, P=O is ~ 0.04 Å longer and the P—O(H) are ~ 0.02 Å shorter than in the free molecule. This is consistent with a resonance hybrid of canonical valence-bond structures that weaken the partial partial double-bond character in the P=O acceptor and strengthen it in the P—OH donor
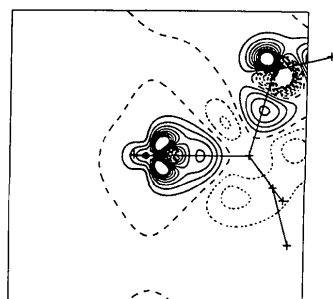
$$\{P{=}O{\cdots}H{-}O{-}P \longleftrightarrow P^+{-}O^-{\cdots}H{-}O{-}P$$

$$\longleftrightarrow P{=}O{\cdots}H{-}O^+{=}P^- \longleftrightarrow etc.\}.$$
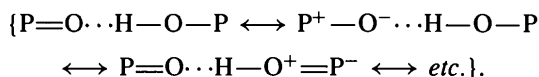
The pseudoatom analysis confirms this picture in two ways. First, the net atomic charges given in Table 4 indicate that P=O is more polarized toward $P^+{-}O^-$ in the experimental crystal structure than in the theoretical simulation by superposition of isolated molecules.
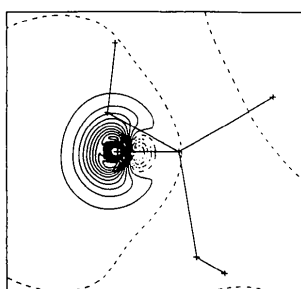
(a)
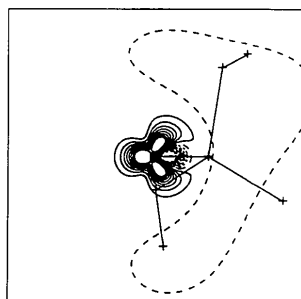
(b)

(c)

Fig. 3. Static deformation density sections from (a) the polarized split-valence molecular wavefunction of Moss *et al.* (1995) and (b) and (c) the experimental pseudoatom fit. (a) and (b) show the section perpendicular to and bisecting the P—O4—H valence angle; (c) shows the section along the P—O4 bond and perpendicular to the P—O4—H plane. Contours as in Fig. 2.

Table 3. *Bond lengths* (Å) *and valence angles* (°) *for the* H_3PO_4 *molecule in the crystal from the experimental diffraction data, and for the molecule in vacuo from the* 6-31G* *geometry-optimized wavefunction of O'Keefe, Domengès & Gibbs* (1985)

E.s.d.'s for the experimental values are 0.001 Å and 0.1°

	Crystal expt.	Free molecule theory		Crystal expt.	Free molecule theory
P=O1	1.493	1.457	O1=P—O2	112.3	
			O1=P—O3	113.1	115.5
P—O2	1.550		O1=P—O4	113.3	
O—O3	1.543	1.573			
P—O4	1.554		O2—P—O3	107.2	
			O2—P—O4	105.7	102.8
O2—H	0.982		O3—P—O4	104.7	
O3—H	0.963	0.951			
O4—H	0.933		P—O2—H	114.2	
			P—O3—H	118.0	123.5
			P—O4—H	113.7	

Table 4. *Net atomic charges* (*electron units*) *from pseudoatom models fitted to simulated static structure factors* (*Moss et al.*, 1995) *and to measured dynamic structure factors* (*this paper*)

	Theoretical data		Experimental data
	q_a	$\langle q \rangle$	q_a
P	+0.049		+0.42 (11)
O1	−0.216		−0.47 (5)
O2	−0.150		
O3	−0.143	−0.144	−0.17 (4)
O4	−0.140		
H2	+0.221		
H3	+0.204	+0.199	+0.19 (3)
H4	+0.173		

Second, the deformation density in the lone-pair regions of the P—O—H groups illustrated in Fig. 3 indicates that hydrogen bonding induces a rehybridization to strengthen the $P^-{=}O^+{-}H$ character. In the isolated molecule [Fig. 3(a)] the P—O—H lone-pair density resembles that in the isolated water molecule (Hermansson, 1984) and appears to occupy a pair of tetrahedral sp^3 orbitals. In the crystal [Figs. 3(b) and (c)], the lone-pair density appears to occupy a trigonal planar sp^2 orbital and a perpendicular $p\pi$ orbital that is polarized toward the P atom.

Whereas we expected that hydrogen bonding would localize the acceptor P=O lone-pair density, we found instead that it relocalized the donor P—O—H lone-pair density. One of the referees of this paper has remarked that we should not have found this surprising, since polarization and exchange repulsion oppose each other at the hydrogen-bond acceptor and reinforce each other at the donor. We hope to investigate this further by additional experimental analyses, at cryogenic temperatures, and by quantum chemical calculations for a hydrogen-bonded cluster at H_3PO_4 molecules.

Appendix

Removing anomalous dispersion effects from Fourier components of the electron density

Near an absorption edge, the atomic scattering factor for X-rays becomes complex

$$f = f^0 + f' + if'' = |f|e^{i\delta} = |f|(\cos\delta + i\sin\delta)$$
$$|f| = [(f^0 + f')^2 + f''^2]^{1/2}$$
$$\delta = \tan^{-1}[f''/(f^0 + f')].$$

The contributions from the wavelength-dependent anomalous dispersion correction terms f' and f'' must be included in structure factor–least-squares calculations of $F_c = |F_c|\exp(i\varphi_c) = A_c + iB_c$ for proper structure refinement, but they must be removed from the measured $|F_o|$ and modeled $|F_c|$ and φ_c for proper electron-density mapping by Fourier synthesis.

Dispersion-free data have sometimes been estimated by multiplying the $|F_o|$ values by the corresponding ratios $|F_c^0|/|F_c|$, where the superscript zero denotes values calculated with $f = f^0$ alone and f' and f'' omitted. This scaling is, however, incorrect because the ratios also multiply the experimental error in the measured $|F_o|$ values and thereby distort the error distribution. If ε represents the net experimental error, including instrumental and statistical errors, in $|F_o| = |F_c| + \varepsilon$, there is no reason to suppose that ε should scale in the same way as $|F_c|$ due to anomalous dispersion. This is especially the case for the relatively weak high-angle reflections, for which both ε and $|F_c| - |F_c^0|$ can be a large fraction of $|F_c|$, the latter because while f^0 values fall off with increasing scattering angle, f' and f'' values remain about constant. Since anomalous dispersion makes an additive contribution to the atomic scattering factors, it should be removed from the crystal structure factors by additive, not multiplicative corrections obtained as follows.

With W_a representing atomic Debye–Waller factors, structure factors

$$F_c(\mathbf{h}) = \Sigma_a|f_a(\mathbf{h})|\exp[i\delta_a(\mathbf{h})]W_a(\mathbf{h})\exp(2\pi i\,\mathbf{h}\cdot\mathbf{r}_a)$$

are calculated from

$$A_c(\mathbf{h}) = \Sigma_a|f_a(\mathbf{h})|W_a(\mathbf{h})\cos[2\pi\,\mathbf{h}\cdot\mathbf{r}_a + \delta_a(\mathbf{h})]$$
$$B_c(\mathbf{h}) = \Sigma_a|f_a(\mathbf{h})|W_a(\mathbf{h})\sin[2\pi\,\mathbf{h}\cdot\mathbf{r}_a + \delta_a(\mathbf{h})]$$

$$|F_c| = (A_c^2 + B_c^2)^{1/2}$$
$$\varphi_c = \tan^{-1}(B_c/A_c),$$

and A and B parts of F_o are

$$A_o = |F_o|A_c/|F_c|$$
$$B_o = |F_o|B_c/|F_c|.$$

Let superscript zero denote A and B parts of F calculated without the anomalous dispersion correction terms. Then

$$A_c^0 = \Sigma_a f_a^0 W_a \cos 2\pi\mathbf{h}\cdot\mathbf{r}_a$$
$$B_c^0 = \Sigma_a f_a^0 W_a \sin 2\pi\mathbf{h}\cdot\mathbf{r}_a$$

$$|F_c^0| = [(A_c^0)^2 + (B_c^0)^2]^{1/2}$$
$$\varphi_c^0 = \tan^{-1}(B_c^0/A_c^0),$$

and

$$A_o^0 = A_o - (A_c - A_c^0)$$
$$B_o^0 = B_o - (B_c - B_c^0)$$

$$|F_o^0| = [(A_o^0)^2 + (B_o^0)^2]^{1/2}$$

$$\sigma(|F_o^0|) = \sigma(|F_o|)[(A_o^0 A_c)^2 + (B_o^0 B_c)^2]^{1/2}/(|F_o^0||F_c|).$$

The $|F^0|$ and φ^0 (or A^0 and B^0) values are the only proper ones to use for Fourier electron-density syntheses

$$\rho(\mathbf{r}) = V^{-1}\Sigma_\mathbf{h}|F^0(\mathbf{h})|\exp[i\,\varphi^0(\mathbf{h}) - 2\pi i\,\mathbf{h}\cdot\mathbf{r}],$$

because for them Freidel's law holds, *i.e.*

$$F^{*0}(\mathbf{h}) = F^0(-\mathbf{h}), \quad |F^0(-\mathbf{h})| = |F^0(\mathbf{h})|$$
$$and \quad \varphi^0(-\mathbf{h}) = -\varphi^0(\mathbf{h}),$$

and, *via*

$$e^{ix} = \cos x + i\sin x,$$

and

$$\cos x\cos y + \sin x\sin y = \cos(x - y),$$

one obtains a real-valued $\rho(\mathbf{r})$ from the generally complex-valued $F^0(\mathbf{h})$

$$\rho(\mathbf{r}) = V^{-1}\Sigma_\mathbf{h}|F^0(\mathbf{h})|\cos[2\pi\mathbf{h}\cdot\mathbf{r} - \varphi^0(\mathbf{h})].$$

References

BECKER, P. J. & COPPENS, P. (1974). *Acta Cryst.* A30, 129–147, 148–153.
BLESSING, R. H. (1988). *Acta Cryst.* B44, 334–340.
BLESSING, R. H. (1989a). *Acta Cryst.* B45, 200.
BLESSING, R. H. (1989b). *J. Appl. Cryst.* 22, 396–397.
BLESSING, R. H. (1995). *Acta Cryst.* A51, 33–38.
CLEMENTI, E. (1965). *IBM J. Res. Dev.* 9, Suppl. As tabulated by STEWART, R. F. & SPACKMAN, M. A. (1983). *VALRAY Users' Manual.* Carnegie-Mellon Univ., Pittsburgh, Pennsylvania.

CROMER, D. T. (1974). *International Tables for X-ray Crystallography*, Vol. IV, pp. 148–151. Birmingham: Kynoch Press. (Present distributor Kluwer Academic Publishers, Dordrecht.) The tabulated f' values need to be adjusted by wavelength-independent corrections given by KISSEL, L. & PRATT, R. H. (1990). *Acta Cryst.* A46, 170–175.

CRUICKSHANK, D. W. J. (1949). *Acta Cryst.* 2, 65–82.

DETITTA, G. T. (1985). *J. Appl. Cryst.* 18, 438–440.

FRENCH, S. & WILSON, K. (1978). *Acta Cryst.* A34, 517–525.

HANSEN, N. K. & COPPENS, P. (1978). *Acta Cryst.* A34, 909–921.

HERMANSSON, K. (1984). *Acta Universitatis Upsaliensis*, p. 744. Doctoral Dissertation, Univ. of Uppsala.

MOSS, G. R., SOUHASSOU, M., ESPINOSA, E., LECOMTE, C. & BLESSING, R. H. (1995). *Acta Cryst.* B51, 650–660.

NELMES, R. J. (1975). *Acta Cryst.* A31, 273–279.

O'KEEFE, M., DOMENGÈS, B. & GIBBS, G. V. (1985). *J. Phys. Chem.* 89, 2304–2309.

STEWART, R. F., DAVIDSON, E. R. & SIMPSON, W. T. (1965). *J. Chem. Phys.* 42, 3175–3187.

ZACHARIASEN, W. H. (1967). *Acta Cryst.* 23, 558–564.

Crystal Structure of the Antiferroelectric Perovskite Pb2MgWO6

BY G. BALDINOZZI AND PH. SCIAU*

Laboratoire de Chimie-Physique du Solide, URA CNRS 453, Ecole Centrale Paris, 92295 Châtenay-Malabry CEDEX, France

M. PINOT

Laboratoire Léon Brillouin, CEA-CNRS, CEN Saclay, 91191 Gif-sur-Yvette CEDEX, France

AND D. GREBILLE

Laboratoire CRISMAT, ISMRA, Bd du Maréchal Juin, 14050 Caen CEDEX, France

Abstract

Lead magnesium tungstate, Pb_2MgWO_6, $M_r = 718.54$. Phase I: cubic, $Z = 4$, $Fm3m$, $a = 8.0058(4)$ Å, $V = 513.1(2)$ Å^3, $D_x = 9.30$ Mg m^{-3} at 350 K, final $R_{wp} = 4.5$ and 7.7%, $R_{Bragg} = 2.9$ and 5.7% for neutron and X-ray powder data, respectively. Phase II: orthorhombic, $Pmcn$ ($Pnma$), $Z = 4$, $a = 7.9440(4)$ and 7.9041(3), $b = 5.6866(3)$ and 5.7035(2), $c = 11.4059(5)$ and 11.4442(4) Å, $V = 515.3(1)$ and 515.9(1) Å^3 at 294 and 80 K, respectively, $D_x = 9.26$ Mg m^{-3} at 294 K. Final $R_{wp} = 4.0$ and 8.5%, $R_{Bragg} = 4.0$ and 9.2% at 294 K and $R_{wp} = 4.0$ and 7.4%, $R_{Bragg} = 2.9$ and 8.4% at 80 K for neutron and X-ray powder data, respectively. To achieve the determination of the structures, X-ray and neutron powder diffraction data were refined together using the Rietveld profile method. The Pb main displacement in the orthorhombic phase from the ideal cubic positions is almost along the $[012]_o$ direction. The O displacements correspond to a weak distortion of the octahedra.

Introduction

The ideal structure of perovskite-type oxide compounds (ABO_3, space group $Pm3m$) is well known and very simple. Its prototype is $CaTiO_3$. It consists of tetravalent B cations at the center of corner-sharing oxygen

octahedra, at the cubic cell origin for example, and divalent A cations at the cell center. In the general family of lead-based perovskites, various compounds have been synthesized by occupying the B site by two species of cation (Galasso, 1990). This leads to the general formula $Pb_2B'_xB''_{1-x}O_6$. Depending on ionic radii and charges, ordering of cations may occur, giving rise to different structural characteristics (different types of superstructure cells, for example) and to various very selective physical properties. The prototype structure of the totally ordered materials consists of a cubic cell with a doubled parameter around 8 Å, and of a centered space group $Fm3m$ resulting from the alternation of cations B' and B''. These perovskite oxides often have very large dielectric permittivities. The degree of long-range order between the species B' and B'' induces different behavior as a function of temperature. Partially or fully disordered compounds exhibit diffuse transitions and relaxor phenomena which are adequate for technological applications (capacitors, actuators, etc.). Ordered compounds present sharper transitions and their sequence of phase transitions is also strongly dependent on the cations involved.

The ordered complex perovskite Pb_2MgWO_6 (PMW) is quite interesting. It undergoes a first-order phase transition from the cubic phase ($Fm3m$) to an orthorhombic antiferroelectric phase at 312 K (Smolenskii, Krainik & Agranovskaya, 1961). The low-temperature phase is

---